International Journal of Biological Macromolecules 315 (2025) 144317

Contents lists available at ScienceDirect

International Journal of Biological Macromolecules

journal homepage: www.elsevier.com/locate/ijbiomac

Delineating the binding site of a series of gold(III) Schiff base chelates on HSA *via* experimentation and *in silico* methods

Sheldon Sookai [a,*], Orde Q. Munro [a,b]

[a] Molecular Sciences Institute, School of Chemistry, University of the Witwatersrand, PO WITS 2050, Johannesburg, South Africa
[b] School of Chemistry University of Leeds, Woodhouse Lane, LS2 9JT, UK

ARTICLE INFO

Keywords:
Albumin
Fluorescence
Stern-Volmer
Ligand binding

ABSTRACT

Human serum albumin (HSA) is crucial for drug transport, influencing pharmacokinetics and pharmacological activity. While drug binding to HSA is well-studied, precise identification of primary binding sites remains underexplored. Since unbound drug fractions impact distribution and receptor-site concentration, understanding HSA interactions is essential for evaluating pharmacokinetics and toxicity. This study presents a systematic workflow integrating fluorescence quenching, circular dichroism, and ligand-binding thermodynamics to map ligand binding on HSA. Using patented Schiff base Au (III) chelates, we validate our approach with experimental data, molecular dynamics simulations, and QM/MM TD-DFT methods. Results indicate all three chelates preferentially bind Sudlow's site I, with affinities following **AuL3** > **AuL1** > **AuL1**, with $logk_a$ values ranging from 4.73 to 5.03. Thermodynamic analysis suggests endothermic, hydrophobic-driven binding. Competitive site displacement assays confirm these findings. Overall, our results highlight HSA's potential as a transporter for metal-based therapeutics and demonstrate the efficacy of our workflow in accurately determining drug-binding sites.

1. Introduction

HSA is the most prevalent plasma protein, with concentrations reaching approximately 0.6 M^{-1} [1]. Two primary functions of HSA are transporting both endogenous and exogenous compounds and regulating colloidal osmotic pressure [2] HSA is a heart shaped protein that consists of a single 585 amino acid polypeptide chain resulting in a molar mass of 66,500 Da [3]. As depicted in Scheme 1b, the redrawn X-ray structure of HSA (PDB: 2BXH) [4] is primarily dominated by α-helices within the three domains, namely I (residues 1–195), II (196–383), and III (384–585). Each domain consists of two subdomains A and B [3,5]. Subdomains IIA and IIIA and are often referred to as Sudlow's site I and Sudlow's site II, respectively, which are the two main small molecule binding sites within the protein [6–8]. HSA is the primary drug transporter in humans and is extensively studied as a potential vehicle for drug delivery, particularly given its ability to be absorbed by cancer cells *in vivo* [9]. In addition to the two primary drug binding sites, HSA contains numerous other binding sites, including seven for fatty acids, four thyroxine, and several known metal ion binding sites [10].

Understanding how a medicinal compound binds to HSA is crucial for interpreting its pharmacodynamic and pharmacokinetic data *in vivo*, due to the abundance of HSA and its role as a transporter in blood plasma [6]. Metallodrug candidates are also involved, with recent studies demonstrating how half-sandwich Ru^{II} and Rh^{III} complexes bind to HSA as intact metal complexes, coordinating to Glu and His residues while retaining the arene structure [11–13]. Typically, protein binding by metal complexes involves ligand dissociation [14–17], while non-dissociative binding is not typical [18–21]. When it does occur, it often relies on multidentate ligands that offer kinetic inertness and thermodynamic stability [22,23], although this is not always the case [24].

A significant body of literature has focused on characterizing small molecules (potential drug candidates) binding to HSA, as this is a fundamental factor in determining a drug's overall pharmacological activity. However, an often-overlooked parameter is identifying the primary binding site of a drug on HSA [6]. Given that the volume of distribution and drug concentration at the receptor site are directly influenced by the fraction of unbound drug, a comprehensive understanding of binding mechanisms to proteins like HSA is essential for evaluating the pharmacokinetic, pharmacodynamic, and toxicological profiles of any drug [25]. Notably, a small molecule with a high affinity for HSA will exhibit a reduced free concentration in plasma [26]. This

* Corresponding author.
E-mail address: Sheldon.sookai@wits.ac.za (S. Sookai).

https://doi.org/10.1016/j.ijbiomac.2025.144317
Received 31 March 2025; Received in revised form 13 May 2025; Accepted 15 May 2025
Available online 20 May 2025

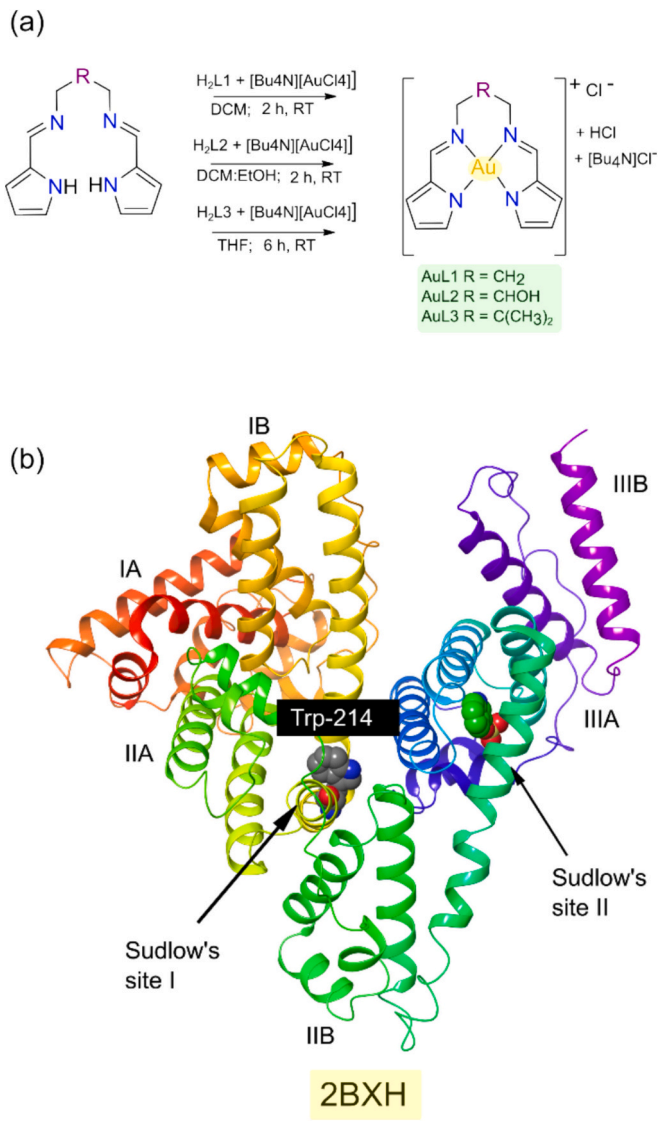

Scheme 1. (a) Representation of the Au(III) metalation of the bis (pyrollide-imine) chelates. (b) X-ray structure of HSA bound to indomethacin (redrawn from PDB code 2BXH [4]) illustrating the two main small molecule binding sites. Sudlow's site I is larger than Sudlow's site II and compounds that bind in this pocket perturb the fluorescence of Trp-214. The protein secondary structure elements are depicted schematically, coloured by domain, and labelled.

high affinity, depending on the specific drug and therapeutic target, can either enhance efficacy by prolonging circulation time or pose a limitation by reducing availability at the target site.

The competition between two drugs for binding to HSA can significantly affect their disposition, potentially leading to serious physiological consequences, particularly when a drug is tightly bound (over 90 %) to HSA [27,28]. A well-documented example is the co-administration of warfarin with phenylbutazone, which increases the risk of hemorrhage in patients. This occurs because phenylbutazone displaces warfarin from its shared binding site on albumin, raising the free concentration of warfarin in plasma [29].

Current methods to identify the binding sites of small molecules on HSA include X-ray crystallography [4]. However, these experiments often fail to mimic physiological conditions, and some ligands may be challenging to crystallize with HSA. As a result, spectroscopic techniques are more commonly employed: (i) Induced Circular Dichroism (CD) Displacement Assay: This method leverages the induced CD signal of an achiral molecule bound to a chiral host, such as HSA [30,31]. The solution is then titrated with site-specific probes, typically warfarin [4,32] for Sudlow's site I or ibuprofen [4] for Sudlow's site II. If the site-specific probe displaces the ligand of interest, the ICD signal diminishes as the displaced ligand returns to an achiral, protein-free state in solution. (ii) Fluorescence Site Displacement Assay: This approach uses the fluorescence quenching properties of site-specific probes, such as warfarin for Sudlow's site I or ibuprofen for Sudlow's site II [4,32]. A ligand of interest is titrated into a solution containing HSA bound to either probe. The site of binding for the ligand of interest is identified based on which HSA-probe complex shows quenched fluorescence.

Gold(III) complexes were initially anticipated to mimic the biological properties of platinum(II) analogues, their redox behavior markedly diverges due to their inherent susceptibility to reduction to Au(I) or elemental Au(0) [33]. This redox lability highlights the critical need for judicious ligand design to stabilize the Au(III) oxidation state and to ensure compatibility with both standard solvents and physiologically relevant media [34,35]. Among the multidentate ligand systems developed for this purpose, CNC-type pincer ligands [36–39], porphyrins [40], and deprotonated pyrroles [41] have proven especially effective. These ligand classes incorporate strong σ-donor atoms (C, N, and O), often in anionic or neutral forms, which complement the hard Lewis acid nature of Au(III) and enhance its resistance to reduction by donating electron density to the metal center [42].

Of particular interest are pyrrole-based Schiff base chelates, which offer both structural versatility and robust coordination properties. These ligands are widely recognized not only for their coordination capabilities but also for their role as pharmacophores in numerous therapeutic agents [43], including FDA-approved drugs such as Tolmetin [44]; Glimepiride [45]; and Sunitinib [46]. Pyrrole-imine metal complexes, a key subclass of Schiff base chelates, exhibit significant medicinal potential. For example, the pentadentate macrocycle texaphyrin [47], known for its ability to chelate Lu(III) [48], has shown promise in photodynamic therapy applications, although it has not yet received FDA approval [49]. The emerging utility of pyrrole Schiff base frameworks in metal complex stabilization and biomedical applications underscores their relevance in the development of gold(III)-based chemotherapeutics.

In this study, we synthesized three patented investigational chemotherapeutic bis(pyrrole-imine) Schiff base Au(III) chelates designated as **AuL1**, **AuL2**, and **AuL3** (Scheme 1). We then explored their binding to HSA using spectroscopic methods under physiological conditions (KH_2PO_4, 50 mM, pH 7.5). The primary objective was to evaluate how structural variations in the carbon chain linking the imine groups influence the chelates' interaction with HSA and to pinpoint their preferred binding site(s).

2. Results and discussion

2.1. Metal chelates synthesis and spectroscopic characterization

We recently reported the synthesis and cytotoxicity of our patented class of Au(III) bis(pyrrolide-imine) Shiff base chelates **AuL1**–**AuL3** [50]. In brief the respective bis(pyrrolide-imine) chelating ligands (**H_2L1**–**H_2L3**) were reacted with [Bu_4N][$AuCl_4$] (Scheme 1b), yielding the desired Au(III) chelate that was obtained as pure precipitates directly from the reaction mixture (Figs. S1–33).

2.1.1. NMR spectroscopy

Recrystallized **AuL1**–**AuL3** were used for spectroscopic characterization of the complexes. The ^{1}H NMR and electronic spectra for **Aul1** is presented and assigned here to highlight the salient spectroscopic features of the Au(III) Schiff base chelates. Figs. 1a and S13 show the ^{1}H and ^{13}C NMR spectra for **AuL1** and reflects coordination of the square planar Au(III) ion by the tetradentate bis(pyrrolide-imine) chelate. The imine proton (N=C–H) resonates as a singlet at 8.27 ppm (CD_3OD), downfield from that of the Pt(II) congener (δH = 8.15 ppm, DMSO-d_6) [52], Pd(II)

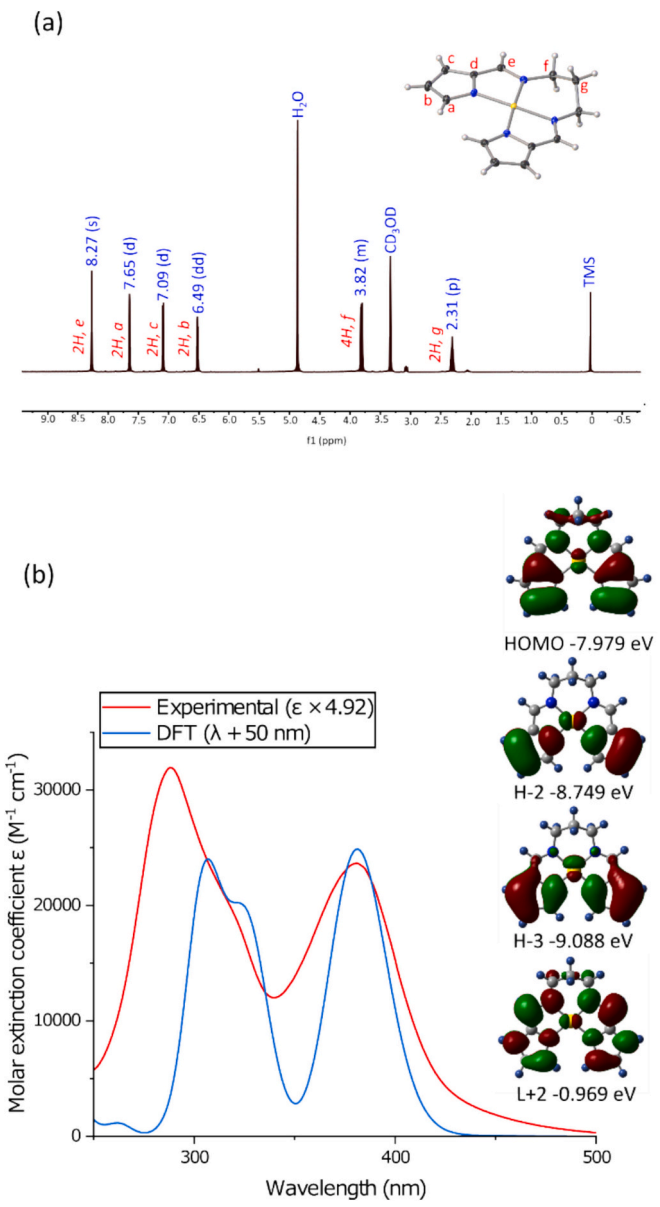

Fig. 1. Spectroscopic characterization and structural assignments for **AuL1**. (a) Proton NMR spectrum (298 K, 400 MHz, CD_3OD). Labelled structure of **AuL** (top right) is a low temperature structure of the complex with the thermal ellipsoids rendered at 50 %, while the H atoms have an arbitrary radius. (b) Electronic spectrum of **AuL1** recorded in methanol. The TD-DFT calculated spectrum scaled (ε and λ) to best match the experimental spectrum is shown with selected transition assignments (band width = 2500 cm^{-1}, fwhm). The HOMO and LUMO frontier MOs are shown. A full list of transition assignments is given in Table S1.

congener (δH = 7.52 ppm, DMSO-d_6) [53], Ni(II) congener (δH = 7.29 ppm, $CDCl_3$) [54] and **H_2L1** in $CDCl_3$ (δ_H =8.03 ppm). The CH signals of **AuL2** and **AuL3** were 8.09 (D_2O) and 8.03 (DMSO-d_6), respectively. This was downfield from **AuL1**, furthermore, differences in solvent polarity led to significant proton chemical shift variations for this class of Au(III) chelates. A systematic trend emerges among the ^{1}H NMR chemical shifts of the imine NH across the d^8 metal ions, following the order: 3d (Ni) < 4d (Pd) < 5d (Pt and Au). This trend indicates that the principal quantum number of the metal ion affects the shielding of the imine proton within the organic ligand framework, with greater electron density leading to upfield shifts. Specifically, the observed shifts are linked to London dispersion forces (LDF), highlighting a correlation with the electronic properties of the metal ion centre [55,56]. The ^{13}C NMR spectrum of **AuL1** was straightforwardly assigned (Fig. S13).

2.2. Electronic spectroscopy

The experimental UV–vis spectrum of **AuL1** is presented in Fig. 1b and was assigned by analysis of the TD-DFT-calculated spectrum of the complex. The analysed spectrum of **AuL1** is representative of the spectra for all three Au(III) chelates. The TD-DFT calculated electronic spectrum of **AuL1** (excluding vibronic transitions), is a fairly good match for the experimental spectrum after we added a 50 nm red-shift correction factor to the band energies and a scaling factor to the intensity's values (ε- 4.92). The visible band at 382 nm (1st excited electronic state) is assigned to assigned HOMO → L + 1 (76 %) and H-1 → L + 2 (14 %); the shoulder transition at 312 nm is decomposed into the following major transitions H-2 → L + 1 (64 %), H-3 → L + 2 (13 %) and H-1 → L + 1 (12 %). Finally, the maximum at 288 nm is the corresponding transition to the 326 nm vibrational level abd is decomposed into H-3 → L + 1 (49 %), H-2 → L + 2 (27 %), H-1 → L + 2 (22 %). The DFT-calculated first excited state at 382 nm is thus 24.5 kJ mol^{-1} higher in energy w.r.t. experiment, even after wavelength scaling.

Analysis of the MOs involved in the transition to the first excited state indicates it comprises 76 % ^{1}[Au(5dyz),π → Au(6pz),π*] character. The unoccupied MO is thus a significantly admixed metal–ligand wavefunction. The shoulder transition band at 312 nm is dominated of 64 % ^{1}[Au($5dx^2-y^2$),π → Au(6pz),π*] character. Finally, the far-UV bands are the most intense with the 288 nm band in the experimental spectrum (ε = 1.67 × 10^4 M^{-1} cm^{-1}) correlating with the 310 nm band of the calculated spectrum. This interesting transition is dominated by MMLCT (metal-to metal– ligand charge transfer) in character, *i.e.*, 64 % ^{1}[Au($5dz^2$) → Au(6pz),π*].

2.3. Importance of delineating the binding site of a ligand on HSA

The interaction of drug candidate compounds (**AuL1**–**AuL3** in this study) and plasma proteins is a key factor in determining their bioavailability [57]. This binding influences the concentration of the free drug, thereby impacting its availability and activity within the body [58]. HSA (the most abundant serum protein) plays a dual role: it can act as a reservoir for therapeutic agents, enabling their availability at concentrations exceeding their plasma solubility, or it can accelerate their clearance, potentially reducing their therapeutic efficacy. These effects are governed by the compound's binding affinity to the protein [59–61]. A strong binding affinity to HSA lowers the concentration of the free drug, thereby extending its half-life, as the bound fraction is less susceptible to hepatic metabolism [59]. Consequently, assessing a drug's interaction with HSA is a critical initial step in understanding its pharmacokinetics and pharmacodynamics, offering valuable insights into its therapeutic potential [6].

HSA has several binding sites throughout the protein but two main small molecule binding sites referred to as Sudlow's sites I and II [6–8]. However, an often-overlooked aspect is determining the primary binding site of a drug on HSA [6]. Since the volume of distribution and drug concentration at the receptor site are directly affected by the fraction of unbound drug, a thorough understanding of protein binding mechanisms, particularly with HSA, is crucial for assessing a drug's pharmacokinetic, pharmacodynamic, and toxicological properties [25]. Numerous studies solely rely on *in silico* methods such as molecular docking or molecular dynamic simulations to predict a ligand binding site on HSA without the use of biophysical data that is often already presented in the study. However, G-scores are unreliable [62], therefore, we present an *in-silico* workflow that utilizes a single protein structure from the PDB and only utilizes empirical data to guide the binding site selection. G-scores are considered solely for choosing a ligand pose within a specific protein site. The method workflow presented in Fig. 2 incorporates UV-CD data, and experimental intrinsic fluorescence

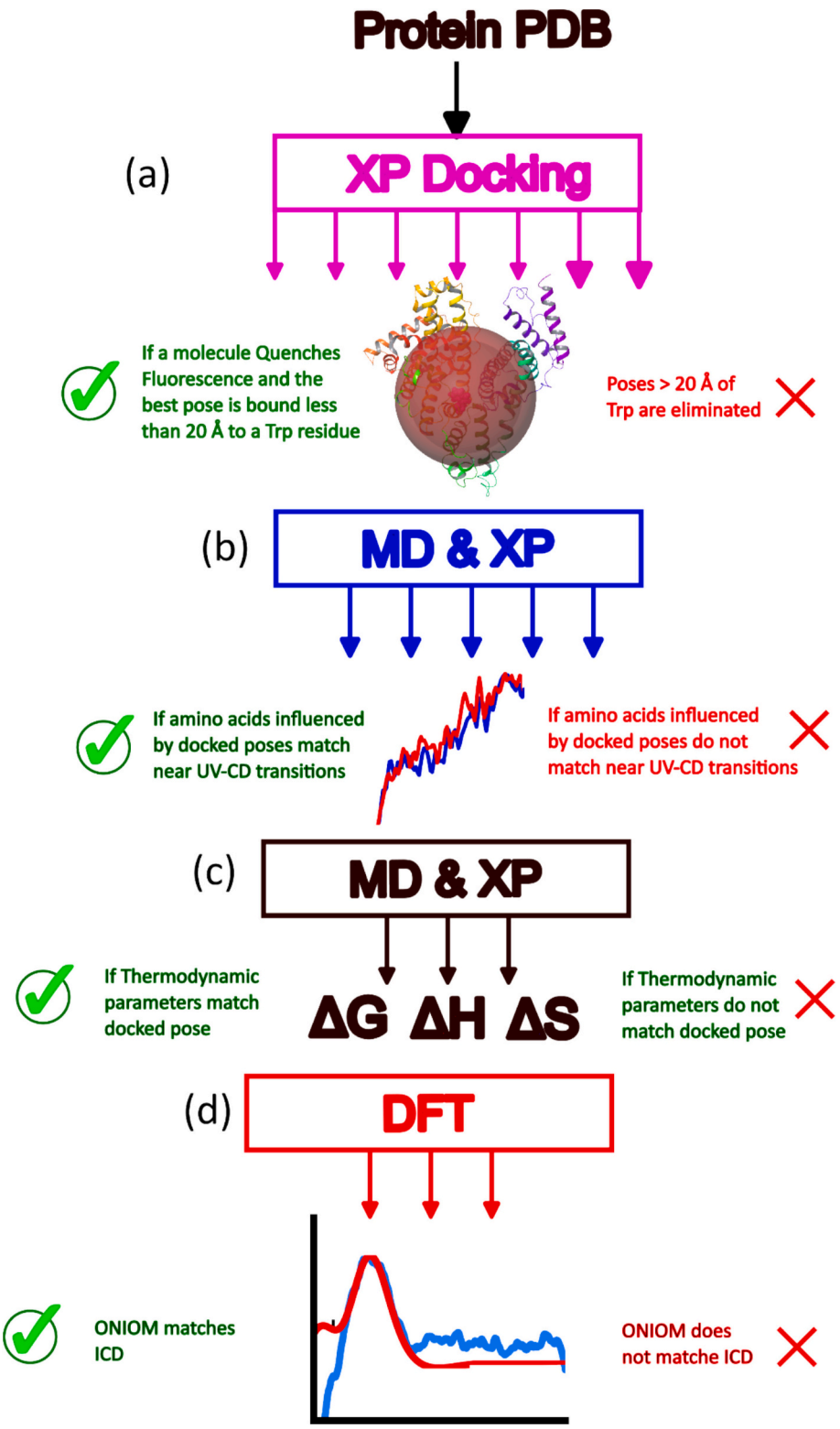

Fig. 2. An *in-silico* workflow that utilizing a single protein structure from the PDB and incorporates UV-CD data and experimental intrinsic fluorescence quenching data to delineate the likely ligand binding sites on HSA. (a) XP docking of the ligand to HSA. (b) XP data is screened against the near UV-CD data. (c) The thermodynamic parameters must be considered. (d) After the final MD equilibration, docked ligands that align with experimental data are selected, and the validated protein–ligand complexes undergo time-dependent DFT (TD-DFT) simulations. After obtained a PDB and performing XP docking each arrow represents a hypothetical number of poses, however, after each experimental screening poses are eliminated. Therefore, the number of poses (arrows) decreases. Finally, a pose can make it to the next screening experiment if it meets the criteria of that step (ticked in green).

quenching data to delineate the likely ligand binding sites on HSA.

The *in-silico* workflow that utilizes a single protein structure from the PDB and incorporates UV-CD data and experimental intrinsic fluorescence quenching data to delineate the likely ligand binding sites on HSA. Fig. 2a; XP docking of the ligand to HSA, poses are screened based on their fluorescence data (*i.e.*, Stern–Volmer (K_{SV}). If the plots exhibit full-range linearity, ligand binding is likely occurring within 15–20 Å of Trp-214 and a single quenching mechanism is dominant. The blue sphere indicates the 20 Å radius cutoff for a ligand to bind, poses exceeding this radius are eliminated as potential binding sites. Poses that pass the first screening are then subjected to MD [63] equilibration and XP docking [64]. The MD trajectory filters out poorly docked ligands, allowing well-docked ones to equilibrate over 100 ns until the protein conformation stabilizes around the ligand. Once equilibrium is reached, the ligand is removed, and XP docking is repeated. This can either enhance the G-score at the same site or, due to the static nature of docking, reveal new binding sites and ligand poses post-MD equilibration. Fig. 2b, show the next experimental screening data is near UV-CD data. If near UV-CD data show perturbation of the disulfide bond (Cys-Cys) upon ligand binding, ligands docked >10 Å away should be excluded. Additionally, near UV-CD data can guide docking constraints; for instance, if the Tyr transitions are affected (275–285 nm), positional restraints can be applied to confine ligand binding within 10 Å of a specific residue. Fig. 2c, shows the thermodynamic parameters must be considered for example if $\Delta S < 0$ we can deduce that disordered water molecules have been displaced, and the ligand must bind within a hydrophobic cavity in the protein. After the final MD equilibration, docked ligands that align with experimental data are selected, and the validated protein–ligand complexes undergo time-dependent DFT (TD-DFT) simulations (Fig. 2d). The HSA·{Ligand} undergoes multilayer ONIOM [65] calculations, with ligands and interacting amino acid residues modelled in a quantum layer using TD-DFT theory, while the proteins amino acid residues are treated using the molecular mechanics layer with force field theory. These calculations generate an induced CD spectrum ICD), which is compared to the experimental ICD spectrum. The protein–ligand complex that best aligns with all empirical data is identified as the experimentally observed system based on fluorescence and CD spectroscopy.

2.4. Fluorescence quenching measurements

The first criterion for delineating the binding site of our metal complex from Fig. 2 requires us to first perform intrinsic fluorescence quenching on the macromolecule to (i) determine the proximity of the ligand to the fluorophore. Therefore, to investigate the mechanism and relative ability of Au(III) chelates to interact with HSA, fluorescence spectroscopy was employed as an informative probe.

When a molecule binds to a protein, it can directly influence the protein's intrinsic fluorescence, which is primarily attributed to three aromatic amino acid residues: tryptophan (Trp), tyrosine (Tyr), and phenylalanine (Phe) [2,66]. Among these residues, Trp contributes most to the intrinsic fluorescence of a protein due to its higher quantum yield and more efficient resonance energy transfer compared to Phe and Tyr [67]. The binding of a molecule to a protein induces changes in the polarity around the fluorophore within the protein, leading to either quenching or enhancement of its intrinsic fluorescence [2]. HSA has a single tryptophan residue (Trp-214) located in subdomain IIA, as well as several tyrosine residues in the protein [67].

We investigated the quenching effect on the intrinsic emission spectrum of HSA (λ^{ex}, 295 nm) by progressively titrating increasing concentrations of Au(III) chelates, ranging from 0 to 97 μM, across a spectral range of 310–400 nm (Fig. 3a). The emission maximum was observed at ~342 nm in KH_2PO_4 buffer (50 mM, pH 7.5), and the intrinsic emission intensity of HSA decreased monotonically with each titration of the respective Au(III) chelates. The fluorescence emission data indicated that all three Au(III) chelates bound to HSA in close proximity, altering the microenvironment around the Trp-214 fluorophore and resulting in its emission being quenched.

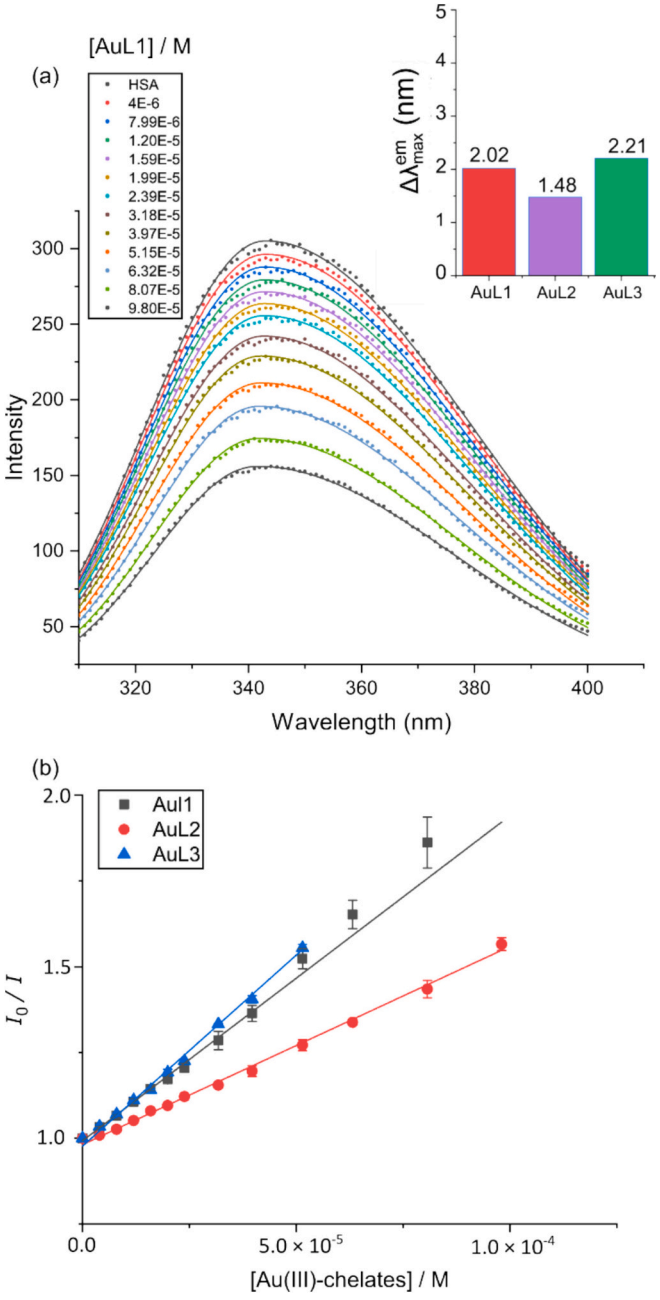

Fig. 3. (a) Emission spectra of human serum albumin (HSA, 5.0 μM) recorded as a function of the concentration of **AuL1** at 298 K in KH_2PO_4 (50 mM, pH 7.50). Analogous spectra for the reaction of HSA with **AuL2** and **AuL3** are given in Fig. S34 (ESI). The wavelength shifts accompanying ligand uptake ($\Delta\lambda^{em}_{max}$) is plotted as the inset to the main figure (upper right). (b) Stern-Volmer (SV) fluorescence intensity ratio plots for human serum albumin (HSA, 5.0 μM) recorded as a function of the concentration of **AuL1**, **AuL2**, and **AuL3** *vs* temperature (50 mM KH_2PO_4, pH 7.50). Error bars are ESDs based on the average of three independent determinations. The data are well-fitted by Eq. (1) for linear Stern-Volmer emission behavior. Analogous spectra for the reaction of HSA with all **AuL3** at 288, 298, and 310 K are given in Fig. S35 (ESI).

The quenching of HSA's intrinsic fluorescence can arise from various mechanisms, including collisional quenching, molecular rearrangements, energy transfer, or ground-state complex formation [68]. Upon binding of the three Au(III) chelates to HSA, the λ^{em}_{max} blue shifts were induced at ~2 nm λ^{em}_{max} for **AuL1**, **AuL3**, λ^{em}_{max} 1.48 nm for **AuL2**, respectively. The blue shift was not as substantial as the blue shift

reported for Pd(PrPyrr) [52], but it suggests that the Trp-214 residue is in a less polar environment after the uptake of the Au(III) chelates [69,70].

Two possible reasons for the λ_{max}^{em} blue shifts are: (i) the orientational polarization of tryptophan caused by ordered water molecules that lie between 15 and 25 Å of the amino acid, and/or (ii) the electronic polarization of the indole ring on the Trp residue due to the binding of the Au(III) chelates. Furthermore, the binding of the Au(III) chelates may induce some electronic polarization of Trp-214, which in turn affects the lowest energy $^1A_1 \rightarrow {}^1L_a$ ground state transition of Trp's indole ring [70]. Ultimately, the similarity in the magnitudes of the measured λ_{max}^{em} shifts indicates that all three Au(III) chelates electronically perturb Trp-214 to the same degree. Regarding the organic framework of the chelating ligands, there is likely charge transfer from the pyrrole ring to the tryptophan indole.

2.5. Fluorescence quenching mechanism

The fluorescence quenching mechanism can be described as either static, dynamic, or a combination of both, and is typically analysed by the Stern–Volmer equation (Eq. (1)), [71].

$$I_0/I = 1 + K_{SV}[Q] = 1 + k_q\tau_0[Q] \quad (1)$$

where I_0 is the fluorescence intensity of HSA in the absence of the added quencher (Au(III) chelates in this work) and I is the fluorescence intensity of HSA in the presence of the Au(III) chelates. K_{SV} is the Stern-Volmer constant (M^{-1}), $[Q]$ is the molar concentration of the quencher (*i.e.*, added Au(III) chelate), k_q is the bimolecular quenching rate constant ($M^{-1}\ s^{-1}$), and τ_0 is the average lifetime of HSA fluorescence in the absence of any quencher (6.72 ± 0.07 ns, [67] 5.60 ± 0.10 ns, [73] and 5.28 ± 0.03 ns; [74] average = 5.87 ± 0.76 ns). Typically, the quenching mechanism can be differentiated by the HSA-Au(III) complex's dependence on viscosity and temperature [75].

From least-squares fits of Eq. (1) to the dose-dependence of I_0/I, the bimolecular fluorescence quenching rate constant for the HSA···Au(III) interaction can be straightforwardly deduced from Eq. (2), provided that τ_0 is known (*vide supra*).

$$k_q = K_{SV}/_{\tau_0} \quad (2)$$

SV plots recorded as a function of temperature and [Au(III)] are presented in Fig. 3b. The plot indicates the average of triplicate results of the mean fluorescence ratio recorded at each dose of Au(III) complex. Typically, Eq. (1) is linear for a single dominant quenching mechanism, either dynamic or static [76,71], the SV plot for all three Au(III) are observed to follow a single dominant quenching mechanism. Notably, the K_{SV} values of the Au(III) chelates increased with increasing temperature, consistent with a dynamic quenching mechanism range [52]. The K_{SV} values increased with increasing temperatures, and this is a result of an increase in the diffusion rate and collisional frequency [78]. The K_{SV} at 298 K values follow the order **AuL1** > **AuL3** > **AuL2**, since the Au(III) metal ion was consistent throughout, the difference in K_{SV} is due to the organic ligand (Fig. 3b). It is important to note that the metal ion plays a major role in in the quenching and binding of compounds to HSA. When comparing the K_{SV} of **AuL1** to the Ni(II), Pd(II) and Pt(II) chelates with the same organic ligand (2,2′-{propane-1,3-diylbis[nitrilo(*E*)methylylidene]}bis(pyrrol-1-ido) the values differed, highlighting the significance of the metal ion centre [52]. A summary of the K_{SV} and K_q values of the interaction of the three Au(III) chelates with HSA is presented in Table 1.

The bimolecular quenching constant (K_q) values were determined for all three Au(III) chelates (Table 1). In each case the K_q exceeded diffusion control limit ($10^{10}\ M^{-1}\ s^{-1}$) [79] by at least two orders of magnitude. This is a strong indication that the binding of the Au(III) chelates was not randomised binding but is consistent with a significant HSA-ligand binding interaction.

Table 1
Stern-Volmer quenching constants (K_{SV}) and bimolecular quenching rate constants (k_q) for the interaction of the three Au(III) chelates with HSA at different temperatures in 50 mM KH_2PO_4 buffer at pH 7.50.

Compound	Temp. T (K)	$10^{-5}\ K_{SV}$ (M^{-1})[a,c]	$10^{-12}\ k_q$ ($M^{-1}\ s^{-1}$)[b]	log (K_a/M^{-1})[c]	n[d]
AuL1	288	1.10 (0.004)	1.82	4.20 (0.07)	1.04 (0.02)
	298	1.17 (0.004)	1.98	4.46 (0.03)	1.11 (0.004)
	310	1.23 (0.010)	2.09	4.73 (0.01)	1.16 (0.01)
AuL2	288	0.56 (0.008)	1.04	4.25 (0.01)	1.13 (0.01)
	298	0.57 (0.003)	0.973	4.37 (0.07)	1.17 (0.02)
	310	0.61 (0.003)	0.979	4.49 (0.04)	1.23 (0.002)
AuL3	288	1.05 (0.004)	1.79	4.60 (0.04)	1.12 (0.01)
	298	1.08 (0.003)	1.84	4.78 (0.08)	1.17 (0.02)
	310	1.10 (0.005)	1.87	5.03 (0.03)	1.23 (0.001)

[a] K_{SV} values (Stern-Volmer constants) for the **AuL1**, **AuL2**, and **AuL3** were determined by fitting the data to Eq. (1).
[b] A mean excited state lifetime, τ_0, of 5.87(76) ns for HSA was used to calculate the bimolecular quenching rate constant, k_q.
[c] The estimated standard deviation of the least significant digits is given in parentheses.
[d] Ligand:HSA binding stoichiometry from the fit of the data to Eq. (3).

The quenching in HSA intrinsic fluorescence as a function of ligand (Au(III) chelate) concentration can be used to calculate the thermodynamic parameters for the binding equilibrium between the protein and Au(III) chelate. The chelates binding affinity towards the protein (K_a) and the stoichiometry (n) are delineated from the double log plot of the quenching of the emission data as a function of the Au(III) chelate concentration (Eq. (3)), [80].

$$log\left(\frac{I_0 - I}{I}\right) = logK_a + nlog[Q] \quad (3)$$

where the intercept and slope of the curve give the affinity constant and stoichiometry, respectively. The data are summarised in Table 1 and has been plotted for all three complexes in Fig. S36. For all Au(III) chelates, the K_a increased with increasing temperatures, which is suggestive that the dynamic quenching mechanism was dominant. [81,80] From Table 1, the logK_a values follow the order **AuL3** > **AuL1** > **AuL2**. All three gold(III)-chelates bound to HSA with a moderate binding affinity ranging from 10^4 to $10^5\ M^{-1}$. The binding affinities were in good agreement of the same complexes measured by ITC that have been previously reported [50].

2.6. UV-CD spectroscopy

Following the determination that the ligands of interest bind within 20 Å of Trp-214 (when excited at 295 nm), our next experimental procedure, based on our proposed binding site criteria (Fig. 2), is near-UV CD spectroscopy (Figs. 4 and S37). Near-UV CD is used to investigate conformational changes induced by ligand binding in the tertiary structure of HSA. We utilized near-UV CD spectroscopy within the 250–310 nm range. Near-UV CD spectra primarily reflect the fine structural features of aromatic amino acid residues, including Trp (285–300 nm), Tyr (275–285 nm), and Phe (250–270 nm). Key transition peaks observed in HSA include two minima at 262 nm and 280 nm, along with a maximum at 290 nm, which are attributed to disulfide bonds and aromatic amino acids [83].

The near-UV CD spectrum of HSA (Figs. 4 and S37) in the absence of Au(III) chelates displayed a peak at 290 nm with fine structural features between 290 and 305 nm, primarily due to the Trp-214 residue. Additionally, within the 275–285 nm range, a peak at 284 nm and a shoulder at 287 nm were detected, likely arising from HSA's Tyr residues. The characteristic Phe fingerprint region (255–270 nm) exhibited a peak at 257 nm. Furthermore, two minima at 262 nm and 268 nm, along with a

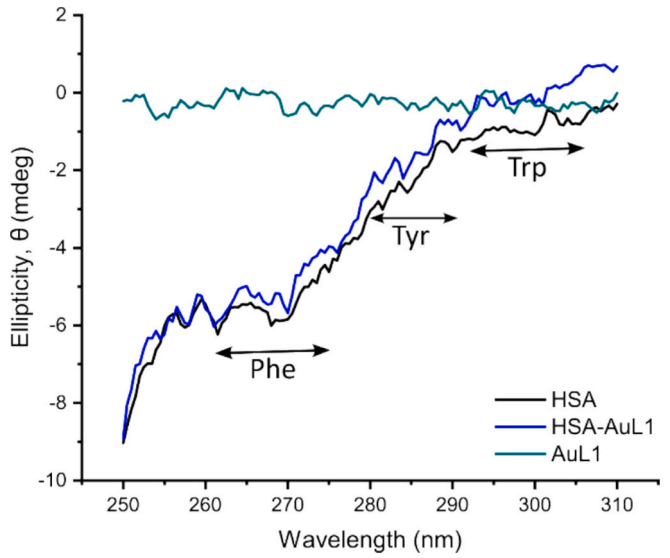

Fig. 4. Plots of the near-UV CD spectra of native HSA and the protein incubated with a 1:1 ratio (6 μM) **AuL1** were recorded at 298 K in 50 mM KH_2PO_4 buffer at pH 7.50. The data represents unsmoothed spectra of the fine structure of the protein. Perturbations in the protein structure around Phe (250–270 nm), Tyr (~280 nm), and Trp (285–300 nm) residues may also be resolved in some different spectra.

shoulder at 279 nm, were indicative of disulfide bonds [84–86], consistent with HSA's 17 disulfide bonds [3]. Phe, Tyr, and Trp possess π–π* transitions (^1L_a and ^1L_b), which enable direct participation in π bonding, a crucial factor in DNA binding. Consequently, alterations in the protein's fine structure may signal conformational changes or the repositioning of aromatic amino acids within a different microenvironment [88].

The introduction of all three Au(III) chelates led to modifications in the near-UV CD spectra, suggesting their binding to HSA in proximity to aromatic residues, particularly Trp and Tyr residues, thereby influencing the fine structure. This finding corroborates the Stern-Volmer quenching data (*vide supra*). Specifically, **AuL1** and **AuL3** caused a 2 nm redshift at 290 nm, whereas **AuL2** led to band splitting at 290 nm along with a 1 nm blueshift. The disulfide bond fingerprint region remained largely unchanged, indicating minimal impact on these bonds. Overall, the binding of Au(III) chelates to HSA resulted in subtle conformational changes in the tertiary structure (Figs. 4 and S37), which may account for the observed enthalpic differences in the van't Hoff plot (*vide infra*) [89].

Based on the near-UV CD data, when performing MD simulations followed by docking (Fig. 2), all poses outside of Sudlow's site I were removed from consideration. Poses within Sudlow's site I were then advanced to part c for screening. A complete analysis of far-UV CD and T_m delineation from far-UV CD is reported in the ESI (Fig. S37).

2.7. Binding thermodynamics

To fulfil our binding site determination protocol (Fig. 2) our next experimental step was the delineation of the ligand's thermodynamic parameters. These parameters were analysed using van't Hoff plot, which provides quantitative thermodynamic data to interpret the major binding forces responsible for the interaction of small molecule-protein interactions [52]. This experiment aimed to use thermodynamic data to screen the best MD-simulated and docked ligand poses, identifying the optimal pose based on all experimental data.

All three Au(III) chelates exhibited a 1:1 reaction stoichiometry with native HSA; consequently, a linear van't Hoff relationship was obtained from the temperature dependence on the K_a values. The plots for triplicate measurements are presented in Fig. 5a. Under non-standard

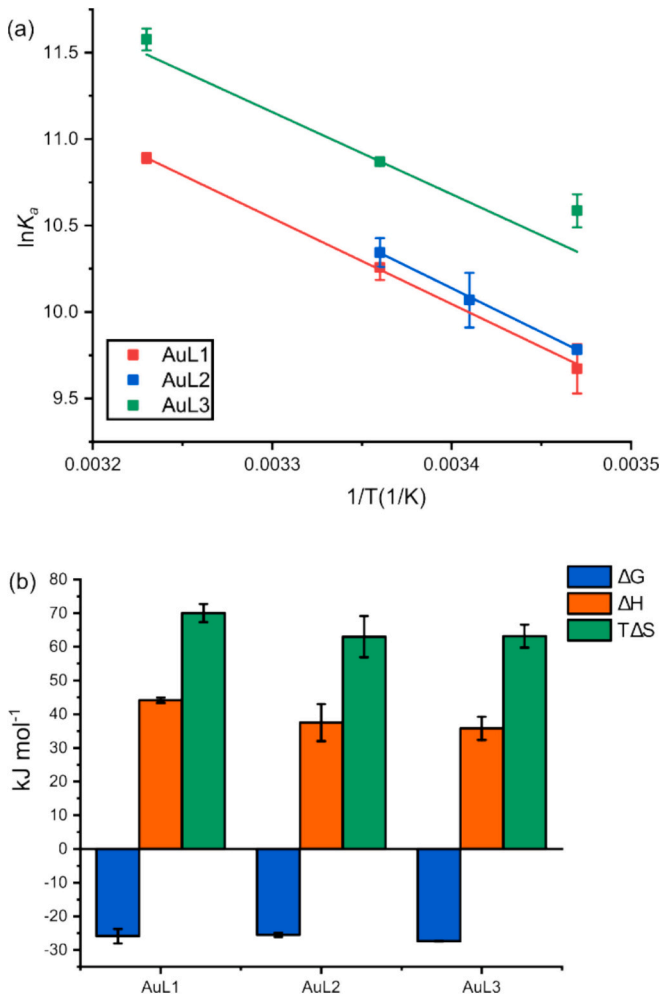

Fig. 5. (a) van't Hoff plots for the reactions of **AuL1** with HSA in 50 mM KH_2PO_4 buffer at pH 7.50. All measurements were done in triplicate; derived parameters were individually averaged, and error bars are estimated uncertainties of the mean. (b) Comparison of the thermodynamic parameters (298 K) governing the reactions of the three Au(III) chelates with HSA.

conditions, the enthalpy change (ΔH), entropy change (ΔS), and Gibbs free energy change (ΔG) can be determined from the temperature dependence of the affinity constants (K_a) using Eqs. (4) and (5):

$$lnK_a = -\frac{\Delta H}{RT} + \frac{\Delta S}{R} \quad (4)$$

$$\Delta G = \Delta H - T\Delta S \quad (5)$$

Table 2
Thermodynamic parameters for the binding of the Au(III) chelates by HSA in 50 mM KH_2PO_4 buffer at pH 7.50.

Compound	T (K)	ΔG (kJ mol^{-1})[a]	ΔH (kJ mol^{-1})[a]	ΔS (J K^{-1} mol^{-1})[a]
AuL1	288	−23.53 (2)		
	298	−25.88 (2)	44.15 (0.8)	−70.03 (3)
	310	−28.70 (2)		
AuL2	288	−23.42 (0.4)		
	293	−24.48 (0.5)	37.50 (5)	−63.02 (6)
	298	−25.53 (0.6)		
AuL3	288	−25.25 (0.1)		
	298	−27.37 (0.1)	35.8 (3)	−63.2 (3)
	310	−29.91 (0.2)		

[a] The estimated standard deviations of the least significant digits are given in parentheses.

Table 2 summarises the van't Hoff thermodynamic data for the reaction of the three Au(III) chelates with HSA in KH_2PO_4 buffer (50 mM, pH 7.5). All three reactions are exergonic (negative ΔG), [80] with ΔG ranging from −28.70 kJ mol^{-1} for **AuL1** to −29.91 kJ mol^{-1} for **AuL3** at 310 K. This is further graphically portrayed in Fig. 5b, where the ΔG values fell in a narrow range for the three Au(III) chelates. The similarity in ΔG is a strongly suggests that the Au(III) chelates bind to HSA (enthalpy/entropy compensation). The minimal energy difference likely reflects the binding of all three Au(III) chelates binding in a similar position within Sudlow's site I (Figs. 7 and S42–43, *vide infra*) in a 1:1 stoichiometric ratio.

The thermodynamic data indicates that both $\Delta H > 0$ and $\Delta S > 0$ which is consistent with entropic control of the reaction. For the Au(III) chelates spontaneity is assured as changes in $\Delta H/\Delta G$ are compensated for by commensurate changes in $T\Delta S/\Delta G$. The $T\Delta S/\Delta G$ and $\Delta H/\Delta G$ of the Au(III) chelates increase together in the order **AuL1** < **AuL2** < **AuL3**.

The observed trend indicates that the thermodynamic parameters of bis(pyrrolide-imine) ligands are influenced by the structural motifs along the carbon chain. Despite all three Au(III) salts being cationic and sharing the same metal center, differences in thermodynamic parameters are primarily driven by the chelating Schiff base. **AuL1** and **AuL3** contain two hydrogen atoms and a dimethyl group moiety on the carbon chain connecting the imine groups in their respective Au(III) chelates. Their primary interactions with HSA arise from the cationic Au(III) center and π–π interactions due to their molecular planarity. In contrast, **AuL2** exhibits similar binding characteristics to **AuL1** and **AuL3** but also includes an OH motif, which enables additional hydrogen bonding interactions.

The ΔH values for the reaction of HSA with the Au(III) chelates are significantly endothermic, measuring from 35.8 kJ mol^{-1} for **AuL3** to 44.15 kJ mol^{-1} for **AuL1**. Fig. 5b highlights the dominance of the entropy term for each of the three reactions, indicating the binding of the three Au(III) chelates to HSA is entropically driven. Interestingly, the differences in the carbon chain linking chains of the respective Au(III) chelates are highlighted in their markedly different ΔH and ΔS values. Specifically, **AuL1** is more endothermic and requires more energy than both **AuL2** and **AuL3** when binding to HSA. This is compensated for by the higher ΔS value for **AuL1** when compared to the other two Au(III) chelates. The trend ΔS values for the Au(III) chelates listed in Table 2 decrease in the following order **AuL1** > **AuL3** > **AuL2** ranging from −70.03 J K^{-1} mol^{-1} (**AuL1**) to −63.02 J K^{-1} mol^{-1} (**AuL2**). The data suggest that the more hydrophilic Au(III) chelates cause substantial desolvation of ordered water molecules within Sudlow's site I on HSA upon binding.

In summation the three Au(III) chelates binding to HSA were endothermically driven, the ΔH and ΔS values were positive suggesting the main binding forces involved with HSA binding to the complexes were *via* hydrophobic interactions [80,90]. The positive ΔH reported is due to two factors, the Au(III) chelates partially destroy the hydrophobic structure within the hydrophobic cavity located in sub domain IIA, which leads to an endothermic effect. The second factor is when the Au(III) chelates enter subdomain IIA within HSA, the initial iceberg structure surrounding the Au(III)-chelates is destroyed [91]. Therefore, when performing the final screen, we can eliminate poses that are dominantly exhibiting electrostatic binding to charged amino acid residues.

2.8. Induced-UV-CD spectroscopy and in silico determination

The phenomenon in which an achiral molecule binds to a chiral host and exhibits a CD signal is known as Induced Circular Dichroism (ICD) [30,92,93]. An ICD band appears at the absorbance wavelength of the chromophoric portion of the complex, indicating direct complexation between the two molecules, as depicted in Fig. 6a.

If the symmetry of an achiral molecule is perturbed and non-zero rotational strengths are formed, it will exhibit an ICD signal [92]. In the context of this study, the Au(III) chelates were initially achiral; however, when bound to HSA, an ICD signal was observed (Figs. 6a and S38). We propose that HSA perturbs the Au(III) chelates through two primary mechanisms: (i) intermolecular interactions and (ii) restriction of conformational freedom [93]. For an ICD signal to arise, the interaction between the protein (host) and the small molecule must occur in a preferred orientation that prevents the cancellation of the ICD signal. Thus ICD serves as a reliable indicator of increased structural order [94,95].

In Fig. 6a, we observe shifts in the ICD bands compared to the absorbance maximum that would be expected for the free Au(III) chelates. An ideal classic supramolecular ICD system involves a non-absorbent, transparent chiral host and an absorbing achiral guest molecule. The Au(III)···HSA system exemplifies the classic example of an ideal supramolecular complex where both HSA and the Au(III) chelates fulfil the requirements of the host and guest molecules respectively [95].

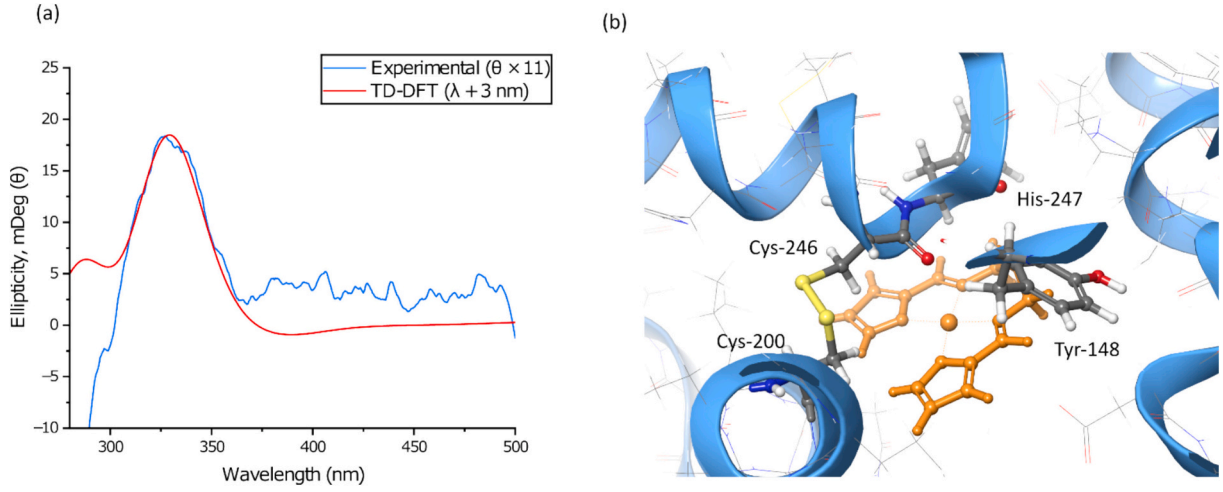

Fig. 6. Comparison of the experimental ICD spectrum (Δθ) recorded for HSA·{**AuL1**} at pH 7.5 in 50 mM (KH_2PO_4) and the CD spectrum calculated using hybrid QM:MM TD-DFT simulations (CAM-B3LYP/SDD/GD3BJ:UFF) for the top-scoring docked pose of **AuL1** bound to Sudlow's site I (PDB code: 1HA2). The DFT-calculated spectrum of the best pose matches the experimental spectrum with great accuracy. (b) View of the metal chelate binding site containing the best pose of both **AuL1** and the closest amino acid residues interacting with the chelate.

The chiral environment of the HSA binding site perturbs the Au(III) chelates, resulting in the induction of rotational strength and an observable ICD signal. The ICD signal manifests as distinct bands in the UV spectrum of the Au(III) chelates, typically around 360 nm. Notably, changes in the chiroptical region of a UV-CD spectrum do not originate from ICD effects. Therefore, near-UV and far-UV CD spectra do not contribute to the ICD signal [96].

The final step in the binding site determination protocol involved selecting the best docked pose from the screening protocol (Fig. 2) and perform a hybrid QM:MM TD-DFT simulations (ONIOM method [97]) to calculate the electronic structures of HSA·{ligand}. The best pose was assigned to the quantum mechanics (QM) layer, and four amino acid residues (Tyr-148, Cys-200, Cys-246, and His-247), interacting with **AuL1** in Sudlow's site I were added to the QM layer for the most accurate ICD spectrum calculation (Fig. 6b). The remaining protein amino acid residues were simulated using molecular mechanics (UFF [98]).

As shown in Fig. 6a, the TD-DFT calculated ICD spectrum of HSA·{**AuL1**} is an excellent match for key spectral features of the experimental ICD spectrum (Fig. 6a). The simulations corroborate all aspects of the experimental data (i) FRET-based quenching of Trp-214 and (ii) location of the ligand within 12 Å of Trp-214 and at least one Tyr residue (highlighted experimentally by the SV plot). (iii) Close proximity binding to a disulfide bridge (< 5 Å; highlighted by the near UV-CD) and finally, (iv) hydrophobic interactions dominating the affinity constants (highlighted by thermodynamic parameters).

2.9. Site displacement assay

To delineate the preferred binding site(s) for the Au(III) chelates, a competitive blocking assay was performed using fluorescence spectroscopy. The Au(III) chelates were titrated into solutions of native HSA and solutions of HSA that were pre-equilibrated with either (i) warfarin

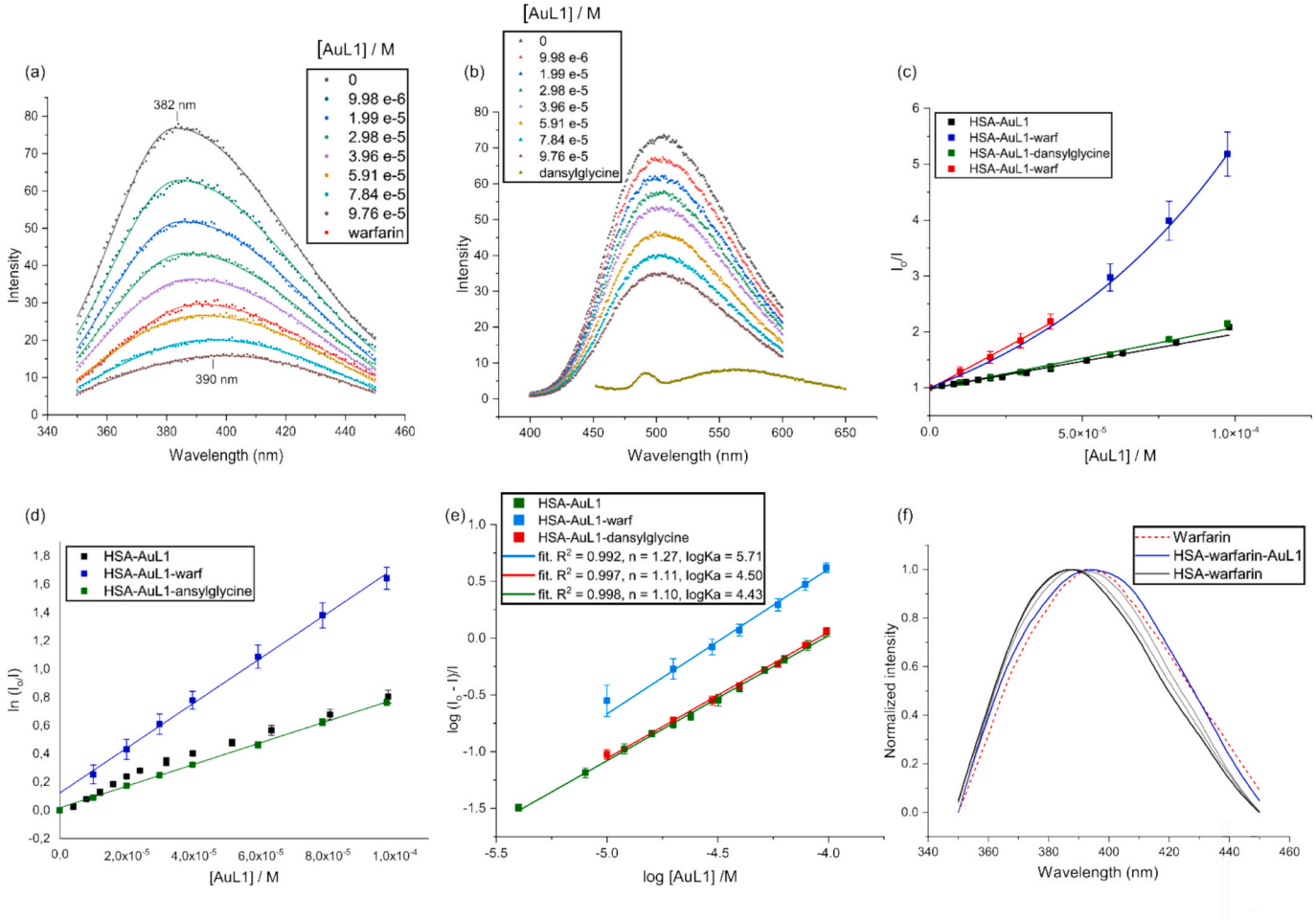

Fig. 7. Binding site determination for the reaction of AuL1 with HSA (5.0 μM protein, 50 mM KH_2PO_4, pH 7.50, 298 K). (a) Emission spectra of HSA···warfarin (5.0 μM warfarin $\lambda^{ex} = 320$ nm) recorded as a function of the concentration of AuL1 at 298 K. The spectra are fitted by single Gaussian functions to locate the emission maxima. Correlation coefficients, R^2, ranged from 0.990 to 0.999. (b) Emission spectra of HSA···dansylglycine (5.0 μM dansylglycine $\lambda^{ex} = 340$ nm) recorded as a function of the concentration of AuL1 at 298 K. The spectra are fitted by single Gaussian functions to locate the emission maxima. Correlation coefficients, R^2, ranged from 0.990 to 0.999. (c) Stern–Volmer (SV) plot for native HSA, HSA···Warfarin, and HSA···dansylglycine as a function of the concentration of AuL1 at 298 K. The plots are linear with an intercept of 1.0 when static quenching is operative (*i.e.*, the quencher binds to the target protein and fluorophore(s)). The excitation and emission wavelengths for the fluorophore probes were: (i) Trp-214 (native HSA), $\lambda^{ex} = 295$ nm, $\lambda^{em} = 340$ nm; (ii) warfarin (HSA-Warf), $\lambda^{ex} = 320$ nm, $\lambda^{em} = 382$ nm, and (iii) dansylglycine, $\lambda^{ex} = 340$ nm, $\lambda^{em} = 500$ nm. (d) Sphere of action model plot, $ln\left(\frac{I_0}{I}\right) = K_{SV}^{app}[Q]$, for the system. A linear plot with a zero intercept indicates static quenching by AuL1 bound in some way to the fluorophore/macromolecule. Negative deviation from linearity signals a switch from static to dynamic quenching. (e) Double-log plot (Eq. (3)) of the fluorescence quenching data, $log\left(\frac{I_0-I}{I}\right) = logK + nlog[Q]$, to enable measurement of $\log K_a$ and the reaction stoichiometry (n). (f) The normalised fluorescence emission spectrum of HSA···warfarin (5.0 μM warfarin $\lambda^{ex} = 320$ nm) recorded as a function of the concentration of AuL1 at 298 K to show the displacement of warfarin from HSA. Error bars indicate the standard deviation of three independent experiments.

or (ii) dansylglycine (Fig. 7). As revealed by X-ray crystallography, warfarin binds specifically in Sudlow's site I (subdomain IIA) [32], while dansylglycine primarily binds in Sudlow's site II (subdomain IIIA) [30]. By selectively and sequentially blocking the two main drug binding sites of HSA using site-specific probes, this experiment aimed to elucidate the binding site specificity of the Au(III) chelates. It should be noted that HSA has multiple drug-binding sites [4], and blocking a primary binding site may redirect the ligand to an alternative drug binding site within HSA or inhibit incoming ligand binding allosterically. Nevertheless, changes in logK_a, n, K_{SV}, and the substitution of the fluorescent probe drug itself could occur upon ligand uptake, allowing for possible deduction of the binding site for the ligand of interest.

The three Au(III) chelates (0–9.76 $\times$ 10^{-5} M) were titrated into a solution of HSA pre-equilibrated with either HSA•{warfarin} or HSA•{dansylglycine}. The fluorescence emission spectrum of both fluorophores is shown in Figs. 7a and S42–43. The HSA•{warfarin} fluorescence emission spectrum peaked at 382 nm, which was a blue shift of 8 nm from the free warfarin peak at 390 nm. Upon titration of the Au(III) chelates into the HSA•{warfarin} solution, the fluorescence intensity of HSA•{warfarin} decreased progressively with increasing concentration of the Au(III) chelates (Figs. 7a, S42, and S43). The percentage displacement of warfarin is illustrated in Fig. S41. Furthermore, the redshift of the warfarin fluorescence emission intensity peak from 382 nm (HSA•{warfarin}) to 390 nm (free warfarin emission peak) provides additional evidence of warfarin displacement from HSA.

The HSA•{dansylglycine} fluorescence emission spectrum peaked at 500 nm, which was a blue-shift of 58 nm from the free dansylglycine peak at 558 nm (Figs. 7b, S55 and S56). Upon titration of the Au(III) chelates into the HSA•{dansylglycine} solution, the fluorescence intensity decreased progressively with increasing concentration of the Au(III) chelates. The suspected percentage displacement of dansylglycine is presented in Fig. S41. Unlike the fluorescence emission spectrum of HSA•{warfarin}, there is no peak shift suggesting dansylglycine is not being displaced from HSA. Quenching of the HSA•{dansylglycine} fluorescence by the Au(III) chelates could reflect quenching by FRET or changing the microenvironment surrounding the fluorophore. To further investigate the binding mechanism of the Au(III) chelates to HSA•{warfarin} and HSA•{dansylglycine}, we used the Stern-Volmer equation (Eq. (1)), the sphere of action model (Fig. S6), and evaluated the binding using the double logarithmic plot (Eq. (3)) (Figs. 7e, S42 and S43).

All three Au(III) chelates bound to HSA *via* a similar mechanism. **AuL1** is discussed as follows. Please refer to Figs. S42 and S43, respectively, for the analyses of **AuL2** and **AuL3**, respectively. From Fig. 7c, the quenching of HSA intrinsic fluorescence and HSA•{dansylglycine} fluorescence resulted in a linear Stern-Volmer plot, indicating a single dominant quenching mechanism. The K_{SV} values of **AuL1** binding to native HSA and HSA•{dansylglycine} were 0.977 (0.032) $\times$ 10^{-5} and 1.105 (0.046) $\times$ 10^{-5} M^{-1}, respectively. Considering the similarity of the K_{SV} values, we predict dansylglycine is not displaced by **AuL1**; rather its fluorescence is quenched by **AuL1** upon its binding to HSA. Interpreting the Stern-Volmer plot of HSA•{warfarin} was more challenging, due to its upward curvature indicating the occurrence of two quenching mechanisms. At concentrations of **AuL1** ranging from 0 to 3.96 $\times$ 10^{-5} M, the plot was linear which we attributed to the static quenching of warfarin, the observed upward curvature is attributed to the displacement of warfarin and its quenching by the aqueous KH_2PO_4 buffer.

To gain further insight into the upward curvature observed in the HSA•{warfarin} Stern-Volmer plot, we applied the "sphere of action model" (Fig. S6). A linear model suggests static quenching, whereas deviation from linearity indicates a transition from static to dynamic quenching mechanisms. From Fig. 7d, only the fluorescence quenching of native HSA showed deviation from linearity. This suggests that **AuL1** acts as a dynamic quencher of HSA intrinsic fluorescence and a static quencher of both HSA•{warfarin} and HSA•{dansylglycine}. Regarding the Stern-Volmer plot for HSA•{warfarin} (Fig. 7c), the initial linear portion could indicate that static quenching is the dominant mechanism. However, as the concentration of **AuL1** increases, the quenching switches from the quenching of HSA•{warfarin} to the displacement of warfarin from HSA, resulting in the quenching of warfarin fluorescence by the aqueous medium.

To gain further insights into the site preference for **AuL1**, we assessed the double log plot (Fig. 7e). Initially, when **AuL1** reacts with native HSA, both Sudlow's sites I and II are available to accept the incoming chelate. Comparing the logK_a values of **AuL1** binding to native HSA and HSA•{warfarin}, we observe that the logK_a value is higher for HSA•{warfarin}, with a value of 5.71 (0.22), compared to 4.43 (0.14) for native HAS (Table 3). Additionally, the logK_a for HSA•{dansylglycine} was 4.50 (0.11), which is one standard deviation away from the logK_a of **AuL1** binding to native HSA. Interpreting the logK_a values can be challenging, and we propose two possible explanations. First, the presence of warfarin in Sudlow's site I may induce conformational changes within the binding pocket, allowing **AuL1** to bind with higher affinity. Second, the value of logK_a for **AuL1** binding to HSA•{warfarin} could be the product equilibrium constant β_2, where $log\beta_2 = logK_1 + logK_2$, where $logK_1 + logK_2 = \log 5.71$.

In summation we believe reporting the site displacement by merely quenching of the extrinsic probes fluorescence is erroneous as quenching may not only occur by displacement of the bound probe but by FRET quenching of the probe as well. This may ultimately lead to incorrectly reporting a ligand may bind to both biding sites on HSA.

2.10. Advantages of using the workflow presented in this manuscript

This study employs a combination of spectroscopic and *in silico* techniques to experimentally characterize the binding interactions between HSA and the ligands under investigation. Compared to purely computational methods like molecular docking or MD simulations which are limited by approximations in scoring functions, rigidity assumptions, and sampling constraints our approach provides direct experimental evidence of binding events, thereby offering greater biological relevance and accuracy.

The suggested workflow in Fig. 2, enhances our ability to investigate HSA-ligand interactions and predict the exact binding site of the ligand to the protein in several keyways: (i) Accuracy: Intrinsic fluorescence quenching allows for the delineation of ligand-to protein binding as well as the elucidation of the thermodynamic parameters of the interaction, in real-time. Binding constants derived from intrinsic fluorescence quenching data are based on measurable physical interactions rather than predictive models. (ii) Sensitivity: The workflow incorporates both intrinsic fluorescence quenching and near UV-CD data, which are highly sensitive, and capable of detecting minute differences in the fluorescence emission of aromatic amino acid residues and the transitions of

Table 3
Stern-Volmer quenching constants (K_{SV}) and binding constant (logKa) for the interaction of **AuL1**, **AuL2** and **AuL3** with HSA, HSA···warfarin and HSA···dansylglycine at 298 K in 50 mM KH_2PO_4 buffer at pH 7.50.

Compound	Temp. T (K)	10^5 K_{SV} (M^{-1})[a,b]	log(K_a/M^{-1})[b,c]
HSA–AuL1	298	1.10 (0.004)	4.43 (0.14)
HSA–AuL1-warfrain	298	2.97 (0.05)	5.71 (0.22)
HSA–AuL1-dansylglycine	298	1.10 (0.1)	4.50 (0.11)
HSA–AuL2	298	0.578 (0.003)	4.37 (0.14)
HSA–AuL2-warfrain	298	3.20 (0.1)	6.19 (0.15)
HSA–AuL2-dansylglycine	298	1.26 (0.03)	4.49 (0.10)
HSA–AuL3	298	1.08 (0.004)	4.78 (0.11)
HSA–AuL3-warfarin	298	2.05 (0.09)	5.35 (0.17)
HSA–AuL3-dansylglycine	298	1.00 (0.03)	4.61 (0.13)

[a] K_{SV} values (Stern-Volmer constants) were determined from fitting the data to Eq. (1).
[b] The estimated standard deviation of the least significant digits are given in parentheses.
[c] Ligand:HSA binding stoichiometry from the fit of the data to Eq. (10).

the aromatic amino acids. This enables the differentiation between strong and weak binders or multi-site interactions. (iii) Site-specific insights: When combined with competitive displacement assays or site-selective probes, the workflow we propose (Fig. 2) can help localize ligand binding to specific sites on HSA, which is often a limitation of non-structural biophysical assays.

Moreover, intrinsic fluorescence quenching and near UV-CD spectroscopy, used in our workflow, are also highly reproducible, protein-sparing, and provide complementary data on protein conformational changes and microenvironment polarity. Their results can corroborate the chromatographic data and provide orthogonal validation. Together, these methods offer a comprehensive, experimentally grounded approach to HSA-ligand interaction analysis, addressing the shortcomings of purely *in silico* methods and allowing researchers to validate or refute computational predictions with confidence.

2.11. Applicability of the method workflow to other proteins and its limitations

The methodological workflow, while initially developed to delineate the binding site of small molecules to HSA, can be adapted to other protein systems. This adaptability is due to several factors:

(i) The spectroscopic techniques used near-UV CD and intrinsic fluorescence quenching rely on aromatic amino acid residues, which are present in virtually all proteins.
(ii) The key criterion for observing an induced circular dichroism (ICD) signal is the restriction of conformational freedom when an achiral small molecule (guest) interacts with a chiral protein (host). This interaction induces a specific and mutual orientation between host and guest, resulting in measurable rotational strengths [94,95]. These interactions represent a classic example of supramolecular complexes, in which the protein acts as a non-absorbing, transparent host, and the small molecule is perturbed by the chiral environment of the protein's binding site [95].
(iii) The *in silico* portion of the workflow relies on molecular docking using the protein's PDB structure, and uses experimental data to eliminate improbable poses, making it applicable to any protein with a high-resolution structure.

3. Limitations

While the workflow is easy to adapt to most proteins, there are some limitations that need to be noted. First, the protein must have been crystallized, and a PDB deposition must be available at high resolution (at least 2.5 Å or better). This ensures a high level of accuracy during XP docking, MD simulations, and ONIOM simulations. A second limitation is that the ligand being analysed in the ligand–protein system must be capable of producing an ICD signal, in order to allow comparison with the ONIOM-calculated spectra in the final step of the workflow.

A third limitation is that not all proteins possess site-specific markers this mainly applies to proteins with multiple ligand-binding sites. Serum albumin proteins, for example, have known site-specific markers such as warfarin [32] and ibuprofen [4], which are used to measure the extrinsic fluorescence of the protein. Therefore, even though one can delineate the exact binding site of a ligand on a given protein using the techniques described in this paper, the data cannot always be corroborated using an extrinsic fluorescence quenching mechanism like that presented in Fig. 7. It should be noted that there are some general site-specific probes, such as 8-Anilinonaphthalene-1-sulfonic acid [100] and SYPRO Orange [101], but these are not designed to mark specific sites. Rather, they generally bind to hydrophobic regions and positively charged amino acid residues of proteins.

4. Conclusion

We present a workflow (Fig. 2) that utilizes both experimental data (fluorescence quenching, near-UV CD, and thermodynamic parameters) and *in silico* data to delineate the binding site of a ligand on the promiscuous serum protein HSA. This was investigated using complementary biophysical spectroscopic techniques to understand how the linking alkyl group of the bis(pyrrole-imine) Schiff base ligand, coordinated to the Au(III) ion, affects the uptake of the complexes by the protein. All three Au(III) chelates quenched the intrinsic Trp-214 fluorescence of HSA, *via* a dynamic quenching mechanism. The three Au(III) chelates had K_a values moderate binding affinity (10^5 M^{-1}). The reaction stoichiometry for all three Au(III) chelates was 1:1 (Au:HSA). Near-UV CD revealed perturbations around Tyr and Trp residues. All three Au(III) chelates bound to HSA endothermically, with positive ΔH and ΔS values, suggesting hydrophobic interactions as the primary binding forces. Using fluorescence quenching, near-UV CD, and thermodynamic parameter data, we screened several top docked poses following MD simulations. Finally, Glide XP docking simulations, combined with ONIOM QM/MM and induced CD site-specificity assays employing probe ligands, demonstrated that all three chelates preferentially bind to Sudlow's Site I. In summary, we present a distinctive approach that integrates *in silico* methods with experimental spectroscopic techniques to identify the preferred binding sites of small molecules on HSA.

CRediT authorship contribution statement

Sheldon Sookai: Writing – review & editing, Writing – original draft, Visualization, Project administration, Methodology, Investigation, Formal analysis, Data curation, Conceptualization. **Orde Q. Munro:** Visualization, Supervision, Software, Project administration, Funding acquisition, Conceptualization.

Author agreement statement

The authors declare that this manuscript is original, has not been published before and is not currently being considered for publication elsewhere.

The authors confirm that the manuscript has been read and approved by all named authors and that there are no other persons who satisfied the criteria for authorship but are not listed.

Declaration of competing interest

The authors declare that they have no known competing financial interests or personal relationships that could have appeared to influence the work reported in this paper.

Acknowledgements

The authors thank WITS University and the NRF for funding to purchase a JASCO J-1500 MCD spectrometer (Grant No 116177, OQM) and a dual-wavelength Bruker D8 Venture X-ray diffractometer (Grant No 129920, OQM). We also thank the Centre for High Performance Computing (Project CHEM1633, CHPC, Cape Town) for both the CPU time and resources needed for the DFT simulations.

Appendix A. Supplementary data

Supplementary data to this article can be found online at https://doi.org/10.1016/j.ijbiomac.2025.144317.

References

[1] S. Curry, Lessons from the crystallographic analysis of small molecule binding to human serum albumin, Drug Metab. Pharmacokinet. 24 (2009) 342–357.

[2] T.P. Jr, All About Albumin: Biochemistry, Genetics, and Medical Applications, Academic Press, 1995, ISBN 978-0-08-052704-8.
[3] X.M. He, D.C. Carter, Atomic structure and chemistry of human serum albumin, Nature 358 (1992) 209–215, https://doi.org/10.1038/358209a0.
[4] J. Ghuman, P.A. Zunszain, I. Petitpas, A.A. Bhattacharya, M. Otagiri, S. Curry, Structural basis of the drug-binding specificity of human serum albumin, J. Mol. Biol. 353 (2005) 38–52, https://doi.org/10.1016/j.jmb.2005.07.075.
[5] P.A. Zunszain, J. Ghuman, T. Komatsu, E. Tsuchida, S. Curry, Crystal structural analysis of human serum albumin complexed with hemin and fatty acid, BMC Struct. Biol. 3 (2003) 6, https://doi.org/10.1186/1472-6807-3-6.
[6] G. Rabbani, S.N. Ahn, Structure, enzymatic activities, glycation and therapeutic potential of human serum albumin: a natural cargo, Int. J. Biol. Macromol. 123 (2019) 979–990, https://doi.org/10.1016/j.ijbiomac.2018.11.053.
[7] G. Sudlow, D.J. Birkett, D.N. Wade, Further characterization of specific drug binding sites on human serum albumin, Mol. Pharmacol. 12 (1976) 1052–1061.
[8] G. Sudlow, D.J. Birkett, D.N. Wade, The characterization of two specific drug binding sites on human serum albumin, Mol. Pharmacol. 11 (1975) 824–832.
[9] Tuan Giam Chuang, U. Kragh-Hansen, M. Otagiri, Pharmaceutical strategies utilizing recombinant human serum albumin, Pharm. Res. 19 (2002) 569–577, https://doi.org/10.1023/A:1015396825274.
[10] M. Fasano, S. Curry, E. Terreno, M. Galliano, G. Fanali, P. Narciso, S. Notari, P. Ascenzi, The extraordinary ligand binding properties of human serum albumin, IUBMB Life 57 (2005) 787–796, https://doi.org/10.1080/15216540500404093.
[11] O. Dömötör, T. Pivarcsik, J.P. Mészáros, I. Szatmári, F. Fülöp, É.A. Enyedy, Critical factors affecting the albumin binding of half-sandwich Ru(II) and Rh(III) complexes of 8-hydroxyquinolines and oligopyridines, Dalton Trans. 50 (2021) 11918–11930, https://doi.org/10.1039/D1DT01700D.
[12] É.A. Enyedy, J.P. Mészáros, O. Dömötör, C.M. Hackl, A. Roller, B.K. Keppler, W. Kandioller, Comparative solution equilibrium studies on pentamethylcyclopentadienyl rhodium complexes of 2,2′-bipyridine and ethylenediamine and their interaction with human serum albumin, J. Inorg. Biochem. 152 (2015) 93–103, https://doi.org/10.1016/j.jinorgbio.2015.08.025.
[13] O. Dömötör, É.A. Enyedy, Binding mechanisms of half-sandwich Rh(III) and Ru(II) arene complexes on human serum albumin: a comparative study, J. Biol. Inorg. Chem. 24 (2019) 703–719, https://doi.org/10.1007/s00775-019-01683-0.
[14] A. Bijelic, S. Theiner, B.K. Keppler, A. Rompel, X-ray structure analysis of Indazolium trans-[tetrachlorobis(1H-indazole)ruthenate(III)] (KP1019) bound to human serum albumin reveals two ruthenium binding sites and provides insights into the drug binding mechanism, J. Med. Chem. 59 (2016) 5894–5903, https://doi.org/10.1021/acs.jmedchem.6b00600.
[15] L. Messori, A. Merlino, Ruthenium metalation of proteins: the X-ray structure of the complex formed between NAMI-A and hen egg white lysozyme, Dalton Trans. 43 (2014) 6128–6131, https://doi.org/10.1039/C3DT53582G.
[16] A. Casini, C. Temperini, C. Gabbiani, C.T. Supuran, L. Messori, The X-ray structure of the adduct between NAMI-A and carbonic anhydrase provides insights into the reactivity of this metallodrug with proteins, ChemMedChem 5 (2010) 1989–1994, https://doi.org/10.1002/cmdc.201000331.
[17] G. Ferraro, M. Paolillo, G. Sciortino, E. Garribba, A. Merlino, Multiple and variable binding of pharmacologically active bis(maltolato)oxidovanadium(IV) to lysozyme, Inorg. Chem. 61 (2022) 16458–16467, https://doi.org/10.1021/acs.inorgchem.2c02690.
[18] F. Wang, J. Bella, J.A. Parkinson, P.J. Sadler, Competitive reactions of a ruthenium arene anticancer complex with histidine, cytochrome c and an oligonucleotide, J. Biol. Inorg. Chem. 10 (2005) 147–155, https://doi.org/10.1007/s00775-004-0621-5.
[19] D. Stanic-Vucinic, S. Nikolic, K. Vlajic, M. Radomirovic, J. Mihailovic, T. Cirkovic Velickovic, S. Grguric-Sipka, The interactions of the ruthenium(II)-cymene complexes with lysozyme and cytochrome c, J. Biol. Inorg. Chem. 25 (2020) 253–265, https://doi.org/10.1007/s00775-020-01758-3.
[20] L. Messori, F.G. Vilchez, R. Vilaplana, F. Piccioli, E. Alessio, B. Keppler, Binding of antitumor ruthenium (III) complexes to plasma proteins, Metal-Based Drugs 7 (2000) 335–342.
[21] A. Casini, C. Gabbiani, E. Michelucci, G. Pieraccini, G. Moneti, P.J. Dyson, L. Messori, Exploring metallodrug–protein interactions by mass spectrometry: comparisons between platinum coordination complexes and an organometallic ruthenium compound, J. Biol. Inorg. Chem. 14 (2009) 761–770, https://doi.org/10.1007/s00775-009-0489-5.
[22] G. Marcon, L. Messori, P. Orioli, M.A. Cinellu, G. Minghetti, Reactions of gold(III) complexes with serum albumin, Eur. J. Biochem. 270 (2003) 4655–4661, https://doi.org/10.1046/j.1432-1033.2003.03862.x.
[23] Y.-C. Lo, T.-P. Ko, W.-C. Su, T.-L. Su, A.H.-J. Wang, Terpyridine–platinum(II) complexes are effective inhibitors of mammalian topoisomerases and human thioredoxin reductase 1, J. Inorg. Biochem. 103 (2009) 1082–1092, https://doi.org/10.1016/j.jinorgbio.2009.05.006.
[24] A. Casini, G. Mastrobuoni, C. Temperini, C. Gabbiani, S. Francese, G. Moneti, C. T. Supuran, A. Scozzafava, L. Messori, ESI mass spectrometry and X-ray diffraction studies of adducts between anticancer platinum drugs and hen egg white lysozyme, Chem. Commun. (2006) 156–158, https://doi.org/10.1039/B611122J.
[25] G.A. Ascoli, E. Domenici, C. Bertucci, Drug binding to human serum albumin: abridged review of results obtained with high-performance liquid chromatography and circular dichroism, Chirality 18 (2006) 667–679, https://doi.org/10.1002/chir.20301.
[26] G. Rabbani, E.J. Lee, K. Ahmad, M.H. Baig, I. Choi, Binding of tolperisone hydrochloride with human serum albumin: effects on the conformation, thermodynamics, and activity of HSA, Mol. Pharm. 15 (2018) 1445–1456, https://doi.org/10.1021/acs.molpharmaceut.7b00976.
[27] U. Kragh-Hansen, Structure and ligand binding properties of human serum albumin, Dan. Med. Bull. 37 (1990) 57–84.
[28] C. Bertucci, E. Domenici, Reversible and covalent binding of drugs to human serum albumin: methodological approaches and physiological relevance, Curr. Med. Chem. 9 (2002) 1463–1481.
[29] S. Harder, P. Thürmann, Clinically important drug interactions with anticoagulants: an update, Clin. Pharmacokinet. 30 (1996) 416–444, https://doi.org/10.2165/00003088-199630060-00002.
[30] F.S. Graciani, V.F. Ximenes, Investigation of human albumin-induced circular dichroism in dansylglycine, PLoS One 8 (2013) e76849, https://doi.org/10.1371/journal.pone.0076849.
[31] S. Sookai, O.Q. Munro, Spectroscopic and computational study of the interaction of Pt(II) pyrrole-imine chelates with human serum albumin, Dalton Trans. (2023), https://doi.org/10.1039/D3DT02039H.
[32] I. Petitpas, A.A. Bhattacharya, S. Twine, M. East, S. Curry, Crystal structure analysis of warfarin binding to human serum albumin: anatomy of drug site I, J. Biol. Chem. 276 (2001) 22804–22809, https://doi.org/10.1074/jbc.M100575200.
[33] A. Casini, C. Hartinger, C. Gabbiani, E. Mini, P.J. Dyson, B.K. Keppler, L. Messori, Gold(III) compounds as anticancer agents: relevance of gold-protein interactions for their mechanism of action, J. Inorg. Biochem. 102 (2008) 564–575, https://doi.org/10.1016/j.jinorgbio.2007.11.003.
[34] A. Casini, L. Messori, Molecular mechanisms and proposed targets for selected anticancer gold compounds, Curr. Top. Med. Chem. 11 (2011) 2647–2660, https://doi.org/10.2174/156802611798040732.
[35] C. Gabbiani, A. Casini, L. Messori, A. Guerri, M.A. Cinellu, G. Minghetti, M. Corsini, C. Rosani, P. Zanello, M. Arca, Structural characterization, solution studies, and DFT calculations on a series of binuclear gold(III) oxo complexes: relationships to biological properties, Inorg. Chem. 47 (2008) 2368–2379, https://doi.org/10.1021/ic701254s.
[36] D. Van der Westhuizen, C.A. Slabber, M.A. Fernandes, D.F. Joubert, G. Kleinhans, C.J. van der Westhuizen, A. Stander, O.Q. Munro, D.I. Bezuidenhout, A cytotoxic bis (1, 2, 3-triazol-5-ylidene) carbazolide gold (III) complex targets DNA by partial intercalation, Chem. Eur. J. 27 (32) (2021) 8295–8307, https://doi.org/10.1002/chem.202100598.
[37] V. Milacic, D. Chen, L. Ronconi, K.R. Landis-Piwowar, D. Fregona, Q.P. Dou, A novel anticancer gold (III) dithiocarbamate compound inhibits the activity of a purified 20S proteasome and 26S proteasome in human breast cancer cell cultures and xenografts, Cancer Res. 66 (2006) 10478–10486.
[38] R.D. Teo, H.B. Gray, P. Lim, J. Termini, E. Domeshek, Z. Gross, A cytotoxic and cytostatic gold(III) corrole, Chem. Commun. 50 (2014) 13789–13792, https://doi.org/10.1039/C4CC06577H.
[39] B. Bertrand, J. Fernandez-Cestau, J. Angulo, M.M.D. Cominetti, Z.A.E. Waller, M. Searcey, M.A. O'Connell, M. Bochmann, Cytotoxicity of pyrazine-based cyclometalated (CˆNpzˆC)Au(III) carbene complexes: impact of the nature of the ancillary ligand on the biological properties, Inorg. Chem. 56 (2017) 5728–5740, https://doi.org/10.1021/acs.inorgchem.7b00339.
[40] C.-M. Che, R.W.-Y. Sun, W.-Y. Yu, C.-B. Ko, N. Zhu, H. Sun, Gold (III) porphyrins as a new class of anticancer drugs: cytotoxicity, DNA binding and induction of apoptosis in human cervix epitheloid cancer cells, Chem. Commun. (2003) 1718–1719.
[41] K.J. Akerman, A.M. Fagenson, V. Cyril, M. Taylor, M.T. Muller, M.P. Akerman, O. Q. Munro, Gold(III) macrocycles: nucleotide-specific unconventional catalytic inhibitors of human topoisomerase I, J. Am. Chem. Soc. 136 (2014) 5670–5682, https://doi.org/10.1021/ja412350f.
[42] L. Messori, F. Abbate, G. Marcon, P. Orioli, M. Fontani, E. Mini, T. Mazzei, S. Carotti, T. O'Connell, P. Zanello, Gold(III) complexes as potential antitumor agents: solution chemistry and cytotoxic properties of some selected gold(III) compounds, J. Med. Chem. 43 (2000) 3541–3548, https://doi.org/10.1021/jm990492u.
[43] V. Bhardwaj, D. Gumber, V. Abbot, S. Dhiman, P. Sharma, Pyrrole: a resourceful small molecule in key medicinal hetero-aromatics, RSC Adv. 5 (2015) 15233–15266.
[44] R.N. Brogden, R.C. Heel, T.M. Speight, G.S. Avery, Tolmetin: a review of its pharmacological properties and therapeutic efficacy in rheumatic diseases, Drugs 15 (1978) 429–450, https://doi.org/10.2165/00003495-197815060-00002.
[45] H.D. Langtry, J.A. Balfour, Glimepiride, Drugs 55 (1998) 563–584, https://doi.org/10.2165/00003495-199855040-00007.
[46] M. Atkins, C.A. Jones, P. Kirkpatrick, Sunitinib maleate, Nat. Rev. Drug Discov. 5 (2006) 279–280, https://doi.org/10.1038/nrd2012.
[47] S. Hannah, V.M. Lynch, N. Gerasimchuk, D. Magda, J.L. Sessler, Synthesis of a metal-free texaphyrin, Org. Lett. 3 (2001) 3911–3914, https://doi.org/10.1021/ol016757s.
[48] J.L. Sessler, T.D. Mody, G.W. Hemmi, V. Lynch, Synthesis and structural characterization of lanthanide(III) texaphyrins, Inorg. Chem. 32 (1993) 3175–3187, https://doi.org/10.1021/ic00066a032.
[49] H. Patel, R. Mick, J. Finlay, T.C. Zhu, E. Rickter, K.A. Cengel, S.B. Malkowicz, S. M. Hahn, T.M. Busch, Motexafin lutetium-photodynamic therapy of prostate cancer: short-and long-term effects on prostate-specific antigen, Clin. Cancer Res. 14 (2008) 4869–4876.
[50] S. Sookai, M. Akerman, M. Færch, Y. Sayed, O.Q. Munro, Cytotoxic pyrrole-based gold (III) chelates target human topoisomerase II as dual-mode inhibitors and interact with human serum albumin, Eur. J. Med. Chem. 287 (2025) 117330, https://doi.org/10.1016/j.ejmech.2025.117330.

[52] S. Sookai, O.Q. Munro, Complexities of the interaction of NiII, PdII and PtII pyrrole-imine chelates with human serum albumin, ChemistryEurope 1 (2023) e202300012, https://doi.org/10.1002/ceur.202300012.
[53] S. Sookai, S. Perumal, M. Kaur, O.Q. Munro, Pt (II) bis (pyrrole-imine) complexes: luminescent probes and cytotoxicity in MCF-7 cells, J. Inorg. Biochem. 258 (2024) 112617–112627.
[54] M.P. Akerman, T. Chatturgoon, O.Q. Munro, An X-ray crystallographic and DFT study of bis(pyrrolide-imine) nickel(II) Schiff base chelates, Inorg. Chim. Acta 421 (2014) 292–299, https://doi.org/10.1016/j.ica.2014.06.015.
[55] O.Q. Munro, G.L. Camp, Self-recognition in a flexible bis(pyrrole) Schiff base derivative: formation of a one-dimensional hydrogen-bonded polymer, Acta Cryst C 59 (2003) o672–o675, https://doi.org/10.1107/S0108270103023230.
[56] O.Q. Munro, S.D. Joubert, C.D. Grimmer, Molecular recognition: preorganization of a bis(pyrrole) schiff base derivative for tight dimerization by hydrogen bonding, Chem. Eur. J. 12 (2006) 7987–7999, https://doi.org/10.1002/chem.200600403.
[57] J. Costa Pessoa, I. Tomaz, Transport of therapeutic vanadium and ruthenium complexes by blood plasma components, Curr. Med. Chem. 17 (2010) 3701–3738.
[58] G. Rabbani, S.N. Ahn, Roles of human serum albumin in prediction, diagnoses and treatment of COVID-19, Int. J. Biol. Macromol. 193 (2021) 948–955.
[59] T. Bohnert, L.-S. Gan, Plasma protein binding: from discovery to development, J. Pharm. Sci. 102 (2013) 2953–2994.
[60] G. Colmenarejo, *In silico* prediction of drug-binding strengths to human serum albumin, Med. Res. Rev. 23 (2003) 275–301, https://doi.org/10.1002/med.10039.
[61] B. Demoro, R.F.M. de Almeida, F. Marques, C.P. Matos, L. Otero, J.C. Pessoa, I. Santos, A. Rodríguez, V. Moreno, J. Lorenzo, R.F. de Almeida, J. Costa Pessoa, D. Gambino, A.I. Tomaz, Screening organometallic binuclear thiosemicarbazone ruthenium complexes as potential anti-tumour agents: cytotoxic activity and human serum albumin binding mechanism, Dalton Trans. 42 (19) (2013) 7131–7146, https://doi.org/10.1039/C3DT00028A.
[62] G.L. Warren, C.W. Andrews, A.-M. Capelli, B. Clarke, J. LaLonde, M.H. Lambert, M. Lindvall, N. Nevins, S.F. Semus, S. Senger, A critical assessment of docking programs and scoring functions, J. Med. Chem. 49 (2006) 5912–5931.
[63] K.J. Bowers, F.D. Sacerdoti, J.K. Salmon, Y. Shan, D.E. Shaw, E. Chow, H. Xu, R. O. Dror, M.P. Eastwood, B.A. Gregersen, et al., Molecular dynamics—scalable algorithms for molecular dynamics simulations on commodity clusters, in: Proceedings of the Proceedings of the 2006 ACM/IEEE conference on Supercomputing - SC '06, ACM Press, Tampa, Florida, 2006, p. 84.
[64] R.A. Friesner, J.L. Banks, R.B. Murphy, T.A. Halgren, J.J. Klicic, D.T. Mainz, M. P. Repasky, E.H. Knoll, M. Shelley, J.K. Perry, et al., Glide: a new approach for rapid, accurate docking and scoring. 1. Method and assessment of docking accuracy, J. Med. Chem. 47 (2004) 1739–1749, https://doi.org/10.1021/jm0306430.
[65] L.W. Chung, W.M.C. Sameera, R. Ramozzi, A.J. Page, M. Hatanaka, G.P. Petrova, T. V. Harris, X. Li, Z. Ke, F. Liu, et al., The ONIOM method and its applications, Chem. Rev. 115 (2015) 5678–5796, https://doi.org/10.1021/cr5004419.
[66] M.-X. Xie, X.-Y. Xu, Y.-D. Wang, Interaction between hesperetin and human serum albumin revealed by spectroscopic methods, Biochim. Biophys. Acta Gen. Subj. 1724 (2005) 215–224, https://doi.org/10.1016/j.bbagen.2005.04.009.
[67] O.K. Abou-Zied, O.I.K. Al-Shihi, Characterization of subdomain IIA binding site of human serum albumin in its native, unfolded, and refolded states using small molecular probes, J. Am. Chem. Soc. 130 (2008) 10793–10801, https://doi.org/10.1021/ja8031289.
[68] S. Sookai, P. Akerman, Q. Munro, O. Chiral, Au(III) chelates exhibit unique NCI-60 cytotoxicity profiles and interactions with human serum albumin, Dalton Trans. 53 (2024) 5089–5104, https://doi.org/10.1039/D3DT04024K.
[69] P.R. Callis, Binding phenomena and fluorescence quenching. II: photophysics of aromatic residues and dependence of fluorescence spectra on protein conformation, J. Mol. Struct. 1077 (2014) 22–29, https://doi.org/10.1016/j.molstruc.2014.04.051.
[70] A. Divsalar, M.J. Bagheri, A.A. Saboury, H. Mansoori-Torshizi, M. Amani, Investigation on the interaction of newly designed anticancer Pd(II) complexes with different aliphatic tails and human serum albumin, J. Phys. Chem. B 113 (2009) 14035–14042, https://doi.org/10.1021/jp904822n.
[71] M.H. Gehlen, The centenary of the Stern-Volmer equation of fluorescence quenching: from the single line plot to the SV quenching map, J. Photochem. Photobiol. C Photchem. Rev. 42 (2020) 100338, https://doi.org/10.1016/j.jphotochemrev.2019.100338.
[73] Helms, Time-resolved fluorescence studies on site-directed mutants of human serum albumin, FEBS Lett. (1997), https://doi.org/10.1016/S0014-5793%2897%2900389-X (Wiley Online Library Available online, accessed on 25 April 2022).
[74] K. Flora, J.D. Brennan, G.A. Baker, M.A. Doody, F.V. Bright, Unfolding of acrylodan-labeled human serum albumin probed by steady-state and time-resolved fluorescence methods, Biophys. J. 75 (1998) 1084–1096, https://doi.org/10.1016/S0006-3495(98)77598-8.
[75] T.K. Maiti, K.S. Ghosh, A. Samanta, S. Dasgupta, The interaction of silibinin with human serum albumin: a spectroscopic investigation, J. Photochem. Photobiol. A Chem. 194 (2008) 297–307, https://doi.org/10.1016/j.jphotochem.2007.08.028.
[76] S. Soares, N. Mateus, V. de Freitas, Interaction of different polyphenols with bovine serum albumin (BSA) and human salivary α-amylase (HSA) by fluorescence quenching, J. Agric. Food Chem. 55 (2007) 6726–6735, https://doi.org/10.1021/jf070905x.
[78] G.G. Ariga, P.N. Naik, S.A. Chimatadar, S.T. Nandibewoor, Interactions between epinastine and human serum albumin: investigation by fluorescence, UV–vis, FT–IR, CD, lifetime measurement and molecular docking, J. Mol. Struct. 1137 (2017) 485–494, https://doi.org/10.1016/j.molstruc.2016.12.066.
[79] J.R. Lakowicz, Principles of Fluorescence Spectroscopy, 3rd ed., Springer US, Boston MA, 2006, ISBN 978-0-387-31278-1.
[80] P.D. Ross, S. Subramanian, Thermodynamics of protein association reactions: forces contributing to stability, Biochemistry 20 (1981) 3096–3102, https://doi.org/10.1021/bi00514a017.
[81] X. Li, S. Wang, Study on the interaction of (+)-catechin with human serum albumin using isothermal titration calorimetry and spectroscopic techniques, New J. Chem. 39 (2015) 386–395, https://doi.org/10.1039/C4NJ01344A.
[83] D. Lafitte, P.O. Tsvetkov, F. Devred, R. Toci, F. Barras, C. Briand, A.A. Makarov, J. Haiech, Cation binding mode of fully oxidised calmodulin explained by the unfolding of the apostate, Biochimica et Biophysica Acta (BBA)-Proteins and Proteomics 1600 (2002) 105–110.
[84] S.M. Kelly, T.J. Jess, N.C. Price, How to study proteins by circular dichroism, Biochimica et Biophysica Acta (BBA) - Proteins and Proteomics 1751 (2005) 119–139, https://doi.org/10.1016/j.bbapap.2005.06.005.
[85] B. Ahmad, S. Parveen, R.H. Khan, Effect of albumin conformation on the binding of ciprofloxacin to human serum albumin: a novel approach directly assigning binding site, Biomacromolecules 7 (2006) 1350–1356, https://doi.org/10.1021/bm050996b.
[86] C. Sun, J. Yang, X. Wu, X. Huang, F. Wang, S. Liu, Unfolding and refolding of bovine serum albumin induced by cetylpyridinium bromide, Biophys. J. 88 (2005) 3518–3524, https://doi.org/10.1529/biophysj.104.051516.
[88] X.-X. Cheng, X.-Y. Fan, F.-L. Jiang, Y. Liu, K.-L. Lei, Resonance energy transfer, pH-induced folded states and the molecular interaction of human serum albumin and icariin, Luminescence 30 (2015) 1026–1033.
[89] N. Zaidi, M.R. Ajmal, G. Rabbani, E. Ahmad, R.H. Khan, A comprehensive insight into binding of hippuric acid to human serum albumin: a study to uncover its impaired elimination through hemodialysis, PLoS One 8 (2013) e71422, https://doi.org/10.1371/journal.pone.0071422.
[90] X. Du, Y. Li, Y.-L. Xia, S.-M. Ai, J. Liang, P. Sang, X.-L. Ji, S.-Q. Liu, Insights into protein–ligand interactions: mechanisms, models, and methods, Int. J. Mol. Sci. 17 (2) (2016) 144, https://doi.org/10.3390/ijms17020144.
[91] J. Grabowska, A. Kuffel, J. Zielkiewicz, Revealing the Frank–Evans "iceberg" structures within the solvation layer around hydrophobic solutes, J. Phys. Chem. B 125 (2021) 1611–1617, https://doi.org/10.1021/acs.jpcb.0c09489.
[92] S. Allenmark, Induced circular dichroism by chiral molecular interaction, Chirality 15 (2003) 409–422, https://doi.org/10.1002/chir.10220.
[93] D. Tedesco, C. Bertucci, Induced circular dichroism as a tool to investigate the binding of drugs to carrier proteins: classic approaches and new trends, J. Pharm. Biomed. Anal. 113 (2015) 34–42, https://doi.org/10.1016/j.jpba.2015.02.024.
[94] G. Gottarelli, S. Lena, S. Masiero, S. Pieraccini, G.P. Spada, The use of circular dichroism spectroscopy for studying the chiral molecular self-assembly: an overview, Chirality 20 (2008) 471–485, https://doi.org/10.1002/chir.20459.
[95] G. Pescitelli, L.D. Bari, N. Berova, Application of electronic circular dichroism in the study of supramolecular systems, Chem. Soc. Rev. 43 (2014) 5211–5233, https://doi.org/10.1039/C4CS00104D.
[96] S.F. Mason, Induced circular dichroism, Chem. Phys. Lett. 32 (1975) 201–203, https://doi.org/10.1016/0009-2614(75)85103-7.
[97] T. Vreven, K.S. Byun, I. Komáromi, S. Dapprich, J.A. Montgomery Jr., K. Morokuma, M.J. Frisch, Combining quantum mechanics methods with molecular mechanics methods in ONIOM, J. Chem. Theory Comput. 2 (2006) 815–826.
[98] A.K. Rappé, C.J. Casewit, K.S. Colwell, W.A. Goddard III, W.M. Skiff, UFF, a full periodic table force field for molecular mechanics and molecular dynamics simulations, J. Am. Chem. Soc. 114 (1992) 10024–10035.
[100] O.K. Gasymov, B.J. Glasgow, ANS fluorescence: potential to augment the identification of the external binding sites of proteins, Biochim. Biophys. Acta 1774 (2007) 403–411, https://doi.org/10.1016/j.bbapap.2007.01.002.
[101] K. Huynh, C.L. Partch, Analysis of protein stability and ligand interactions by thermal shift assay, Curr. Protoc. Protein Sci. 79 (2015) 28.9.1–28.9.14, https://doi.org/10.1002/0471140864.ps2809s79.